Synthesis and Application of Ferroelectric P(VDF-TrFE) Nanoparticles in Organic Photovoltaic Devices for High Efficiency

Zhengguo Xiao, Qingfeng Dong, Pankaj Sharma, Yongbo Yuan, Baodong Mao, Wenjing Tian, Alexei Gruverman, and Jinsong Huang*

The power conversion efficiency (PCE) of organic photovoltaic devices has entered the over 10% era.[1,2] Interlayers between the organic active layer and the electrodes play important roles in achieving high efficiencies. Many types of interlayers have been reported, such as metal oxides,[3–5] polymer electrolytes,[6,7] and low-work-function metals.[8] Generally, these interlayers have the function of bridging the Fermi energy of the electrode and the energy levels of the organic semiconductor and increasing the built-in electric field in the devices.[6] Recently, we reported a new category of air stable material, ferroelectric polymer poly(vinylidenefluoride-trifluoroethylene) (P(VDF-TrFE)), as a universal interlayer, which has tunable and high-density, aligned dipoles controlled by the external applied bias.[9] This ferroelectric interlayer can effectively increase or decrease the work function of any electrode to serve as both anode and cathode due to the switchable dipole direction. A strong electric field can be induced in the semiconducting polymers by the unscreened polarization charges of the P(VDF-TrFE), which has been demonstrated to improve the PCE of several types of organic photovoltaic cells (OPVs) to unprecedented values, superior to many other methods. In our previous studies, it was also shown that the polarization of P(VDF-TrFE) on the organic semiconductor films is stable[10,11] and the surface charges are not screened by photogenerated carriers.[10]

A crystalline β-phase P(VDF-TrFE) film is needed to ensure its ferroelectricity.[10] Langmuir-Blodgett (LB) deposition is an excellent method for forming highly crystalline P(VDF-TrFE) film as thin as 1 nm.[9] However, P(VDF-TrFE) LB films generally need a thermal annealing process after the deposition to convert them into the ferroelectric phase at above the Curie temperature. In our previous studies, the P(VDF-TrFE) 70:30) LB films were annealed at 135 °C for half an hour to completely convert them to the ferroelectric phase.[9,11] However, this high temperature thermal annealing process is not compatible with the fabrication process of many high-performance, low bandgap polymer-based OPV devices, such as thieno3,4-b-thiophene/benzodithiophene (PTBs)[6,12,13] and poly N-9′-hepta-decanyl-2,7-carbazole-alt-5,5-(4′,7′-di-2-thienyl-2′,1′,3′benzothiadiazole) (PCDTBT).[14–16] These polymers are generally heated at 70 °C or vacuumed to remove solvent in the spun films.[14] A high-temperature annealing at 135 °C will significantly reduce the PCEs of these polymer-based OPVs due to over annealing, causing overly large 6,6-phenyl-C_{61}-butyric acid methyl ester (PCBM) or polymer nanodomains.[17] In addition, it is difficult to control the morphology of P(VDF-TrFE) LB films after thermal annealing.[18] Appropriate P(VDF-TrFE) size of the nanoislands and spacing between them is critically important so that the photogenerated charges can be fully extracted rather than blocked by the large, thick insulating P(VDF-TrFE) nanoislands.[9] In an optimal scenario, the size of the P(VDF-TrFE) nanoislands should not exceed the diffusion length of the electrons in donor:$PC_{70}BM$ (6,6-phenyl-C_{71}-butyric acid methyl ester) films.

Despite the huge need for P(VDF-TrFE) nanostructures for many applications, such as bistable memory devices,[19] actuators,[20] mechanical-energy-harvesting devices,[21] and many others, there is no universal method for the fabrication of P(VDF-TrFE) nanostructures with a facile process. In previous reports, nanostructures have been primarily constructed by electrospinning,[22] nanoimprinting,[19,23] and template methods.[24–26] However, such methods are not scalable for producing large quantities of P(VDF-TrFE) nanomaterials. In addition, these nanostructures are too large for ferroelectric organic photovoltaic (FE-OPV) applications.

In this work, we report the preformation of ferroelectric P(VDF-TrFE) 50:50) nanoparticles (NPs) by a solution chemistry method and their application in low bandgap polymer photovoltaic devices to avoid high-temperature, post-deposition thermal annealing. To the best of our knowledge, this is the first time that ferroelectric polymer NPs are synthesized by a simple solution method and applied in FE-OPVs. The size and crystallinity of P(VDF-TrFE) NPs can be easily controlled before they are inserted into the polymer solar cells. The coverage of

Z. Xiao, Dr. Q. Dong, Dr. Y. Yuan, Dr. B. Mao,
Prof. J. Huang
Department of Mechanical and Materials Engineering
University of Nebraska
Lincoln, NE 68588, USA
Z. Xiao, Dr. Q. Dong, P. Sharma, Dr. Y. Yuan,
Dr. B. Mao, Prof. A. Gruverman, Prof. J. Huang
Nebraska Center for Materials Nanoscience
University of Nebraska
Lincoln, NE 68588, USA
P. Sharma, Prof. A. Gruverman
Department of Physics and Astronomy
University of Nebraska
Lincoln, NE 68588–0299, USA
Prof. W. Tian
State Key Laboratory of Supramolecular Structure and Materials
Jilin University
Changchun, 130012, P. R. China
E-mail: jhuang2@unl.edu

ADVANCED
ENERGY
MATERIALS

www.advenergymat.de

Materials Views

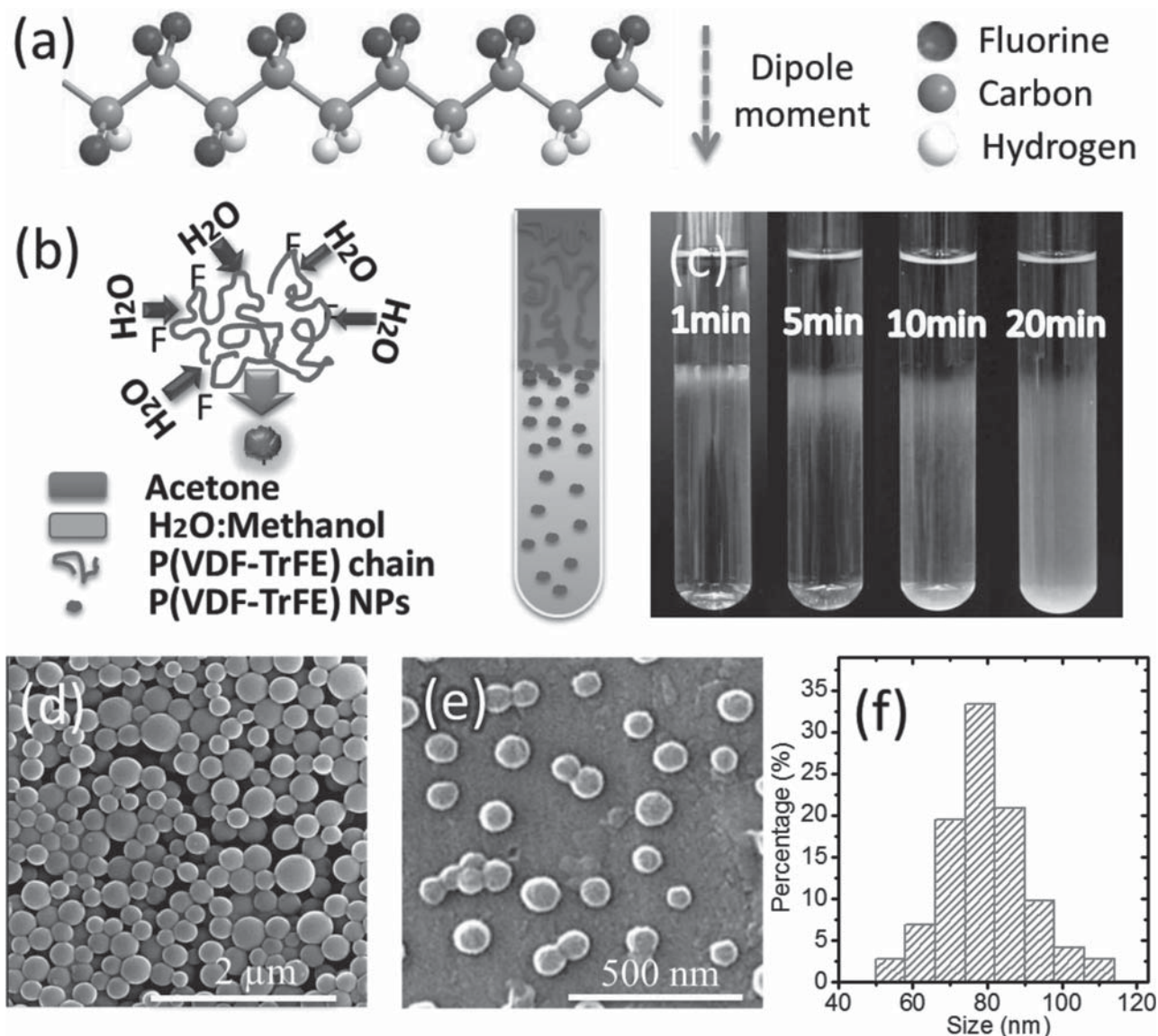www.MaterialsViews.com

COMMUNICATION

Figure 1. a) Chemical structure of P(VDF-TrFE). b) Schematic process for the synthesis of P(VDF-TrFE) nanoparticles (NPs). c) Pictures of formation process of P(VDF-TrFE) NPs with different reaction time using acetone as good solvent and pure water as poor solvent. SEM images of P(VDF-TrFE) as-grown NPs using water as the poor solvent (d) and water:methanol (1:10 v/v) blend solvent as the poor solvent (e). f) P(VDF-TrFE) NP size distribution based on 71 NPs.

the P(VDF-TrFE) ferroelectric interlayer can then be precisely manipulated to maximize the efficiency of FE-OPVs. In addition, it is easy to deposit the P(VDF-TrFE) NPs using a low-cost, scalable solution process, such as spray coating and spin coating. The average PCE of the PCDTBT: $PC_{70}BM$ device with P(VDF-TrFE) NPs after positive poling achieved 6.50%. The best PCE reached 6.64%, which is among the highest values reported for PCDTBT-based solar cells.[14,27,28]

The chemical structure of the P(VDF-TrFE) co-polymer used in this study is shown in **Figure 1**a. There is a large dipole moment point from the fluorine to the hydrogen side in the ferroelectric P(VDF-TrFE) due to their electron affinity difference. The P(VDF-TrFE) NP formation principle is illustrated in Figure 1b, which is a hydrophobic-interaction-induced polymer

self-organizing method. P(VDF-TrFE) was dissolved in a good solvent of acetone, and then a poor solvent, such as water, was injected into the acetone. P(VDF-TrFE) NPs form at the interface of good and poor solvents by the diffusion of P(VDF-TrFE) to the solvent interface, and the NPs were precipitated out by the high speed centrifuge at a speed of 20 000 rpm for 10 min. The details of the synthesis process are described in the Experimental Section.

The strong hydrophobic interaction between water and fluorine in P(VDF-TrFE) leads to the aggregation of P(VDF-TrFE) chains and forms NPs. The hydrophobic interaction is mostly an entropic effect originating from the disruption of highly dynamic hydrogen bonds between water molecules by the nonpolar solute.[29] Because the P(VDF-TrFE) chain cannot form
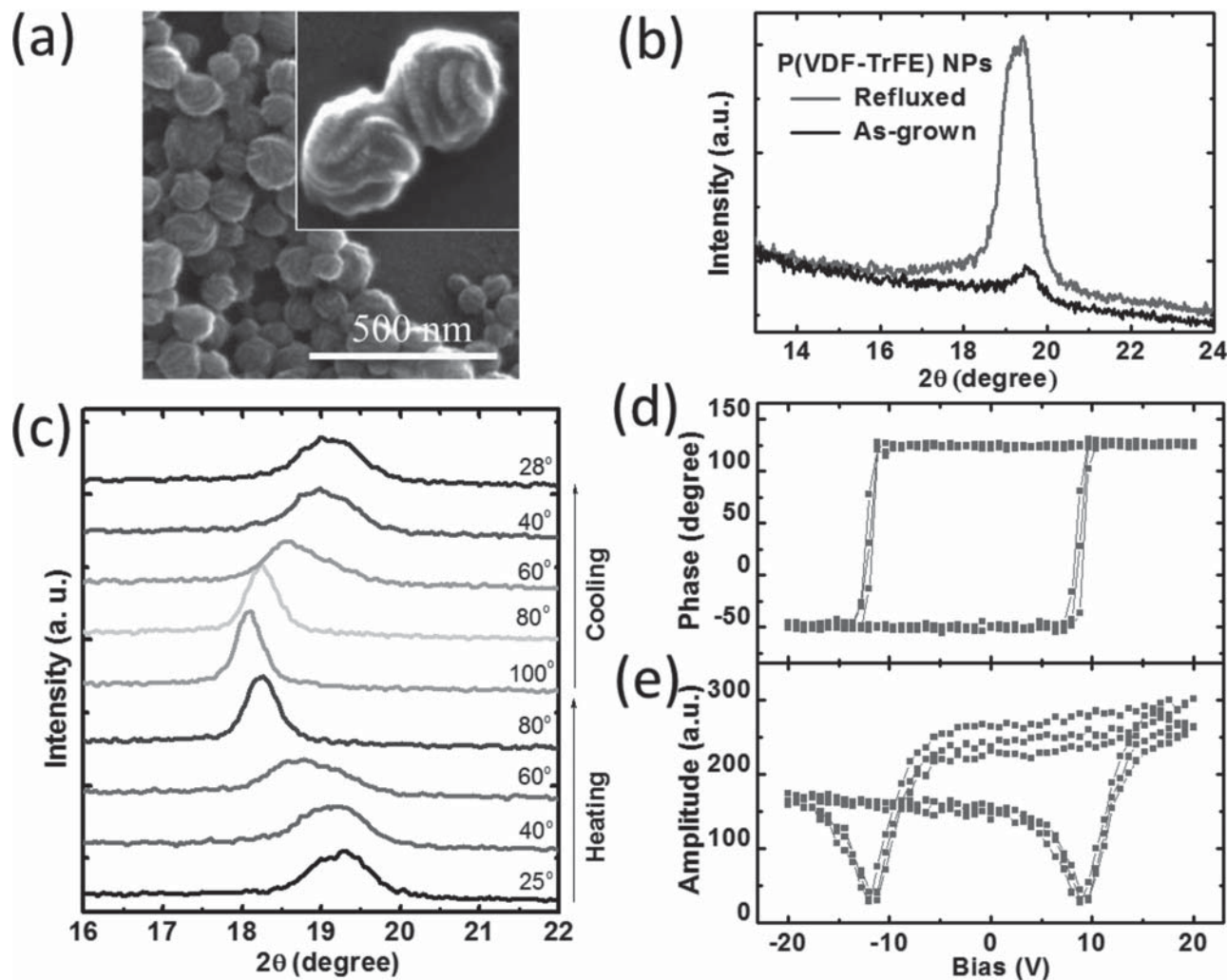
Figure 2. a) SEM image of the refluxed P(VDF-TrFE) NPs. Inset: enlarged image of the NPs. b) XRD of the as-grown P(VDF-TrFE) NPs and refluxed P(VDF-TrFE) NPs. c) XRD of the refluxed P(VDF-TrFE) NPs under various temperatures. d,e) Non-linear hysteresis loop (phase and amplitude) of a refluxed P(VDF-TrFE) NP on top of Au covered silicon substrate.

hydrogen bonds with water molecules, P(VDF-TrFE) molecules tend to aggregate to the NPs to reduce the surface area exposed to water. Figure 1c shows how P(VDF-TrFE) NPs typically form at the acetone and water interface. After injection of water from the bottom, the water/acetone interface forms. P(VDF-TrFE) molecules dissolved in acetone diffuse to the interface to form NPs, and the NPs move down to the water phase by gravity. The tuning of the polarity (and solubility) difference changes the size of the NPs. Adding methanol into the water can reduce the polarity difference between the good and bad solvents, and the average size of NPs can be reduced from 300–500 nm using pure water down to 60–90 nm using a water:methanol ratio of 1:10 (Figure 1d,e). The statistical size distribution of the P(VDF-TrFE) NPs is shown in Figure 1f.

The as-grown NPs are expected to be relatively amorphous, which was demonstrated using the X-ray diffraction (XRD) measurements. In order to obtain crystalline ferroelectric P(VDF-TrFE) NPs that can be used in FE-OPV devices, the P(VDF-TrFE) NPs dispersed in water:methanol were refluxed at 90 °C, which is

above its Curie temperature of 65 °C,[30] for 60 min. **Figure 2**a shows the scanning electron microscopy (SEM) image of refluxed NPs, which show a very different surface morphology from the as-grown smooth spherical NPs. The P(VDF-TrFE) surface is rough with a clear laminar/dendrite structure. As shown in Figure 2a, all the refluxed P(VDF-TrFE) NPs are expected to be converted into the ferroelectric phase to some extent because every nanoparticle shows laminar/dendrite textures.

The dramatically improved crystallinity of P(VDF-TrFE) NPs after refluxing was confirmed by XRD measurement which shows much stronger, sharp (110)-(200) peaks[31,32] compared to the as-grown NPs, as shown in Figure 2b. The calculated lattice spacing for the d(110) peak is 0.46 nm which agrees with previous reported value of the β-phase co-polymer P(VDF-TrFE) with 50% TrFE.[33] In order to further confirm the present phase is β-phase, we measured the XRD pattern of the refluxed P(VDF-TrFE) NPs film under various temperatures from room temperature (RT) to 100 °C which is above its curie temperature of 65 °C. As shown in Figure 2c, a second XRD peak,
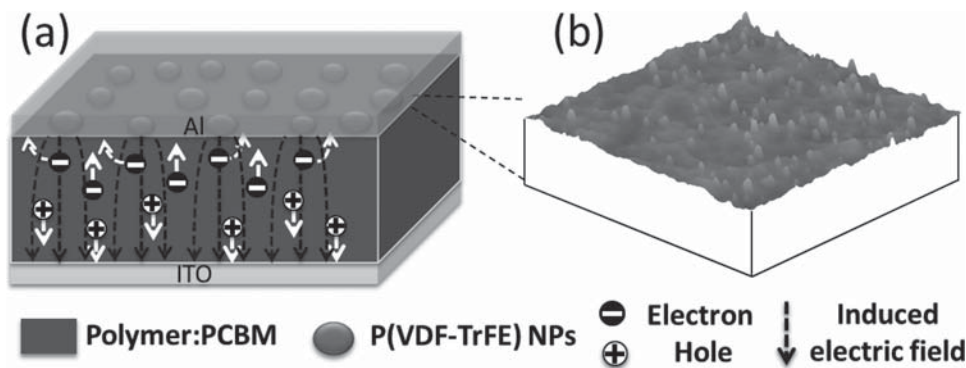
ADVANCED
ENERGY
MATERIALS

www.advenergymat.de

Materials Views

www.MaterialsViews.com

COMMUNICATION

Figure 3. Schematics of FE-OPV device working mechanism. a) After reverse bias poling, the unscreened surface charges of the P(VDF-TrFE) NPs will generate electric field and penetrate through the organic active layer, which will help the extraction of photogenerated charges. b) 3D AFM image of topology of NPs on the organic active layer surface with scale of 5 μm × 5 μm.

corresponding to the paraelectric α-phase, starts to appear at 65 °C, which is close to the paraelectric–ferrelectric transition temperature. The peak shifts from 19.2° at RT to 18.2° after heating the film to 80 °C, indicating the conversion of the P(VDF-TrFE) NP film into a pure paraelectric α-phase. As expected, the diffraction peak shifts back to 19.1° after cooling the film back to RT.

The most straightforward method to verify the ferroelectricity of the P(VDF-TrFE) NPs is to measure the polarization hysteresis loop (P–E) loop. It is however difficult to fabricate a continuous and pin-hole free thin film with the refluxed P(VDF-TrFE) NPs without resorting to thermal annealing due to their relative large size and irregular shape. To address this issue, we used piezoresponse force microscopy (PFM) to directly measure the piezoelectric hysteresis loops of individual NPs. Figure 2d,e show saturated hysteresis loops of refluxed P(VDF-TrFE) NPs measured by PFM on top of gold covered silicon substrate. It is clearly seen that the polarization of the refluxed P(VDF-TrFE) NPs is switched by the voltage bias supplied by the PFM tip, confirming the ferroelectricity of the P(VDF-TrFE) NPs.

Figure 3 shows schematics of the working mechanism of FE-OPV devices with P(VDF-TrFE) NPs as the interlayer. After positive poling under reverse bias, the unscreened polarization charges of P(VDF-TrFE) NPs on the organic active layer side will generate a large electric field pointing from the cathode to the anode. This large electric field will enhance the bound charge pair separation and increase the charge extraction efficiency.[9] The 3D AFM image of P(VDF-TrFE) NPs on top of PCDTBT:PC$_{70}$BM film is shown in Figure 3b. In polymer:PCBM bulk heterojunction solar cells, electron diffusion lengths ranging from 40–130 nm have been reported, depending on the property of the polymer and content of PCBM.[34] Small P(VDF-TrFE) NPs of 60–90 nm were selected as the ferroelectric interlayer so that most photogenerated carriers can go around the insulated NPs by diffusion and be collected by the electrode.

We first studied the influence of the crystallinity of P(VDF-TrFE) NPs on the performance of an FE-OPV by comparing the photocurrents of the devices with as-grown amorphous P(VDF-TrFE) NPs and refluxed crystalline P(VDF-TrFE) NPs as interlayers at the cathode. **Figure 4**a,b show their photocurrent curves under a 100 mW cm^{-2} Air Mass 1.5 Global (AM1.5)

illumination. There is almost no poling effect for the device with the amorphous NPs, which can be explained by their nonferroelectric nature (or switchable dipoles). In contrast, the PCE of the device with crystalline P(VDF-TrFE) NPs increased by 23% after positive poling, as shown in Figure 4b. This result clearly demonstrates that the crystallinity of P(VDF-TrFE) is critical for the improvement of FE-OPV performance because only the crystal ferroelectric P(VDF-TrFE) has large density, aligned dipoles. The influence of the crystallinity of P(VDF-TrFE) nanostructures on the poling effect in FE-OPVs was highlighted by comparing the short circuit current density (J_{sc}) variation under different poling voltages of the devices with as-grown amorphous P(VDF-TrFE) NPs and refluxed crystalline P(VDF-TrFE) NPs. Here, the poling voltage was increased gradually from –1 V to –8 V. As shown in Figure 4c, the J_{sc} of the device with refluxed P(VDF-TrFE) NPs increased gradually with applied negative bias from –5 V to –7 V, and nearly saturated at –8 V, while the J_{sc} of the device with as-grown NPs remained almost unchanged. The crystalline refluxed NPs were then used for the following study.

There should be an optimized coverage of P(VDF-TrFE) NPs for a maximized PCE because of the trade-off between the induced electric field and the increased series resistance (R_s) by the insulating P(VDF-TrFE) NPs. We continuously varied the density of P(VDF-TrFE) NPs on the PCDTBT:PC$_{70}$BM surface by tuning the concentration of the NP solution as well as the spin speed. **Figure 5**a–e show the J–V curves and the corresponding SEM images with different NP coverage, and **Table 1** summarizes the variation in the device parameters, including J_{SC}, V_{OC} (open circuit voltage), FF (fill factor), PCE, R_s, and shunt resistance (R_{sh}) for the devices with different P(VDF-TrFE) NP density. For each category of devices, both the average device efficiency and best device efficiency are listed. When the NPs are very sparse, with a coverage of 2%, the positive poling of the P(VDF-TrFE) NPs caused almost no change to the photocurrent, as shown in Figure 5a. However, the R_s is relatively low, around 1.3 ohm cm^{-2}. The poling effect becomes obvious when the P(VDF-TrFE) NP coverage is increased to 5%. The PCE increased from 4.4% to 5.0% after poling, while the R_s increased to 3.0 ohm cm^{-2}.

There is a clear trend of device performance variation with the P(VDF-TrFE) NP density. With P(VDF-TrFE) NP density increasing, the series resistance before poling increases and
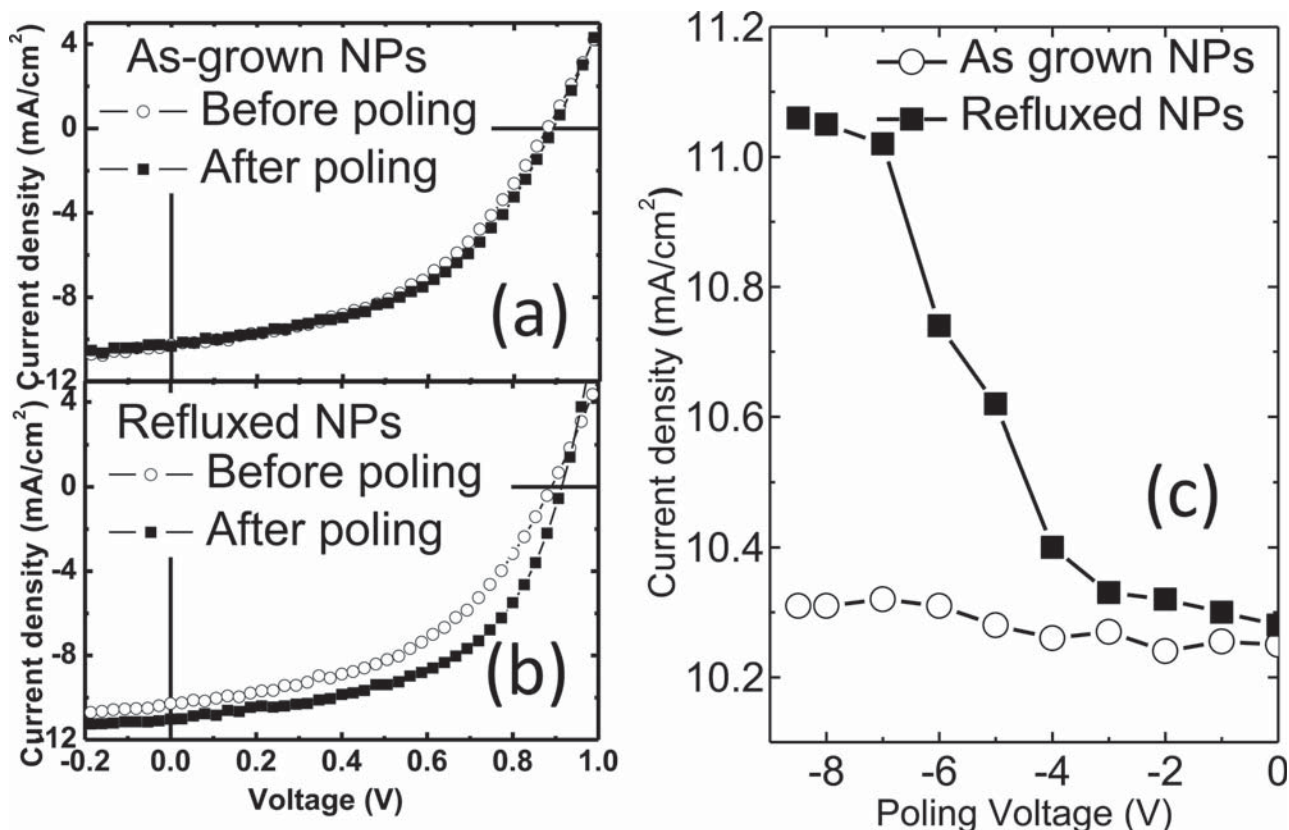
COMMUNICATION

Figure 4. The photocurrent curves of PCDTBT:PC$_{70}$BM based device with the as-grown amorphous NPs (a), and the refluxed ferroelectric P(VDF-TrFE) NPs (b) before (open circles) and after poling (squares). c) J_{sc} variation with poling voltage for the device with the as-grown amorphous NPs (open circles) and the refluxed ferroelectric P(VDF-TrFE) NPs (squares) after poling.

the poling effect becomes increasingly distinct. When the P(VDF-TrFE) NP coverage was increased to 38%, the insulating NPs greatly increased the series resistance of the device to 8.4 Ω cm^{-2}. Although the PCE increased by 144% after poling the dense P(VDF-TrFE) NPs, the total PCE was low, only 2.2%. The optimized NP coverage was found to be around 18%, which is larger than the nanomesa coverage of an annealed two monolayer LB film (coverage: 15%). The best PCE increased from 4.74% to 6.64% after poling.

One unique characteristic of FE-OPVs is that the photocurrent of the device can be switched with a high voltage pulse. As shown in Figure 5f, the FE-OPV device, after a reverse bias poling, has larger J_{sc}, V_{oc}, FF, and PCE than the as-obtained device. The photocurrent was switched back to the low PCE state with a relatively small forward bias of 5 V. Here, a small forward bias was used to avoid the burning of the device. We also compared the device performance of FE-OPVs with P(VDF-TrFE) NPs as the cathode interlayer and the regular devices with Ca/Al as the cathode. The efficiency of the optimized devices with Ca/Al as the cathode had a PCE of 5.19%, which is comparable to those reported elsewhere.[35] The larger J_{sc} of FE-OPV after positive poling was also confirmed by its external quantum efficiency (EQE), as shown in the inset of Figure 5f. The highest EQE reached 70% in the optimized FE-OPV device. The superior performance of FE-OPVs can be understood by the reduced charge recombination in the devices

with P(VDF-TrFE) NPs which is reflected by their larger shunt resistance, higher J_{sc}, and FF, as shown in Table 1. After positive poling, the induced electric field is expected to increase the drift length of the carriers and/or extend the charge bimolecular recombination lifetime.[9] The series resistance of P(VDF-TrFE) NPs is, however, still larger than that of the device with Ca/Al as the cathode even with optimized NP spacing due to the insulating nature of the device with P(VDF-TrFE) NPs.

In conclusion, we demonstrated the synthesis of ferroelectric P(VDF-TrFE) NPs and their application in enhancing the PCE of low bandgap polymer-based solar cells for the first time. A clear dependence of the device performance on the induced electric field was revealed by controlling the poling voltage as well as P(VDF-TrFE) NP coverage. Compared to the LB method, this method gives better control of the P(VDF-TrFE) coverage, which is critical for optimizing the performance of FE-OPVs. With the denser P(VDF-TrFE) nanoislands obtained by this method, a larger electric field, around 20 ± 3 V μm^{-1} in PCDTBT:PC$_{70}$BM film, can be induced by the P(VDF-TrFE) NPs, which is 50–100% higher than the electric field generated by the 1–2 monolayer LB P(VDF-TrFE). After optimization of coverage of P(VDF-TrFE) NPs, the average PCE of a PCDTBT:PC$_{70}$BM-based solar cell reached 6.5%, i.e., 25% higher than the control devices with Ca/Al as the cathode. Our devices were highly reproducible and the PCE was averaged over 50 devices. It is believed that this kind of P(VDF-TrFE)
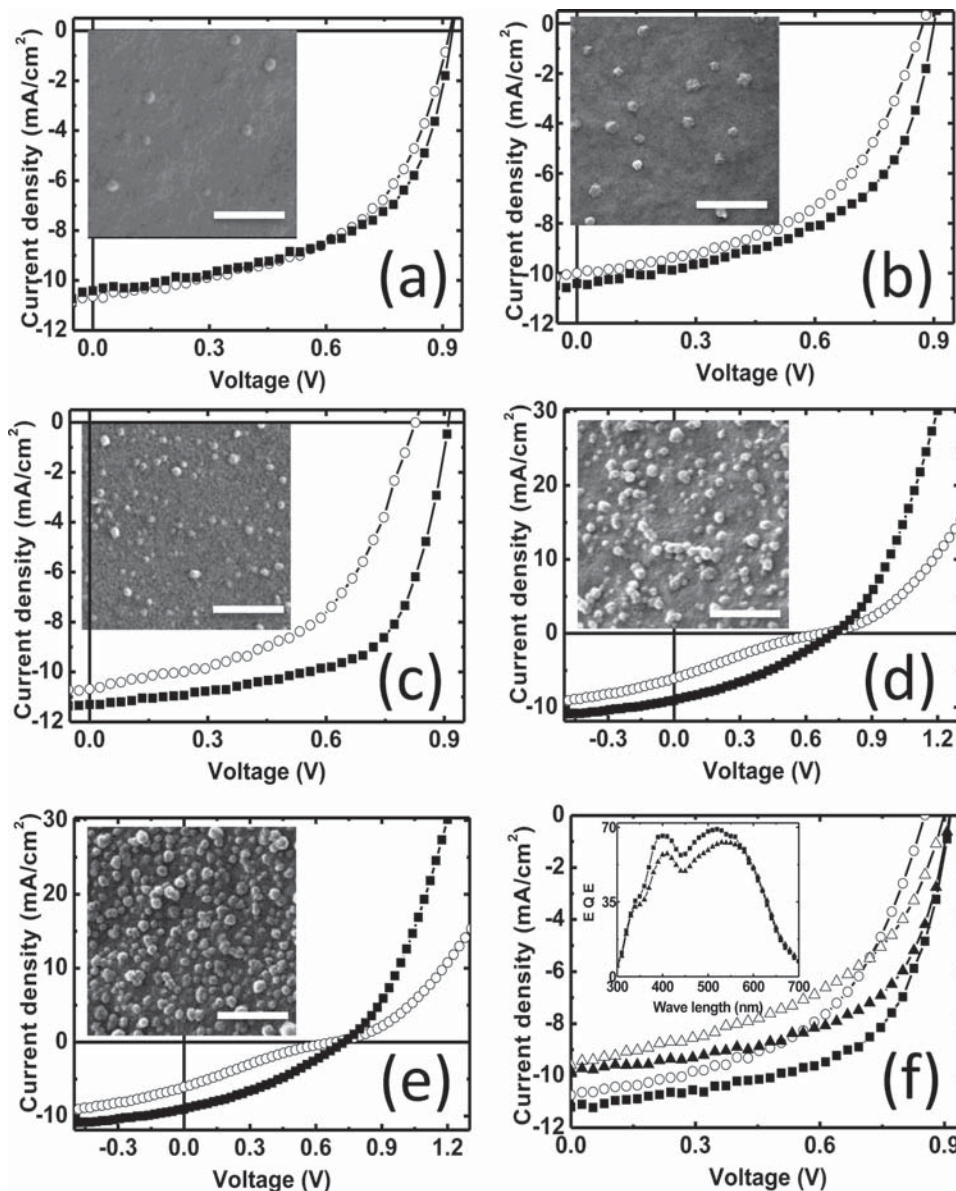
ADVANCED
ENERGY
MATERIALS
www.advenergymat.de

COMMUNICATION

Materials
Views
www.MaterialsViews.com

Figure 5. a–e) Photocurrents of the FE-OPV devices before (open circles) and after poling (squares), which have P(VDF-TrFE) NPs on top of active layer with increasing coverage. The corresponding SEM images of P(VDF-TrFE) NPs distribution are shown as insets. Scale bars in all the SEM images are 1 μm. f) Photocurrent curves of the FE-OPV device with P(VDF-TrFE) NPs as interlayer without poling (open circles), after positive poling (squares), after negative poling (open triangles) and controlled device with Ca/Al as cathode (triangles). The EQE curves of the devices with P(VDF-TrFE) NPs after positive poling (squares) and with Ca/Al cathode (triangles) are shown in the inset.

NP can be broadly applied in other low bandgap polymers to improve PCE because they do not need post-deposition thermal annealing.

Experimental Section

Synthesis P(VDF-TrFE) Nanoparticles: Poly(vinylidenefluoride-trifluoro-ethylene) P(VDF-TrFE 50:50) NPs were prepared by a self-organizing process at the interface of two solvents with different polarity. P(VDF-TrFE) was dissolved in good solvent (acetone) with a concentration of 5 mg mL^{-1}. Water was added to methanol to make a water:methanol blend solution with varied volume ratio which is a poor solvent for

P(VDF-TrFE). The methanol was used to tune the polarity of the poor solvent and stabilize the reaction, which would lead to more uniform and smaller size NPs. Both solvents were cooled down to 0 °C before use.

First, the 2 mL P(VDF-TrFE) acetone solution was injected into a 10 mL centrifuge tube. Then, 0.5 mL of pure acetone and 4 mL of the water:methanol blend solution were injected into the tube from the bottom. The 0.5 mL of pure acetone was used as a buffer layer, which can stabilize the reaction and avoid severe aggregation of P(VDF-TrFE) while injecting the water:methanol. An interfacial layer was formed between the acetone and the water:methanol blend solution. The P(VDF-TrFE) molecules diffused to the interface of the good and poor solvents and connected with water. The hydrophobic interaction between P(VDF-TrFE) and water led self-assembling P(VDF-TrFE) molecules to form NPs.

www.MaterialsViews.com

ADVANCED
ENERGY
MATERIALS
www.advenergymat.de

COMMUNICATION

Table 1. Comparison of FE-OPV performances with different ferroelectric P(VDF-TrFE) NP density before and after positive poling at −7 voltage. The performance of the device with Ca/Al as cathode and optimized NPs spacing was averaged over 50 devices, and the performance devices with other NP spacing were averaged over 10 devices.

P(VDF-TrFE) NPs coverage		J_{sc} [mA cm^{-2}]	V_{oc} [V]	FF	R_s [Ω cm^2]	R_{sh} [Ω cm^2]	PCE %	PCE % (best)
With Ca/Al (no NPs)		9.8	0.91	58.0	1.00	479	5.19 ± 0.10	5.29
2%	Before poling	10.6	0.91	53.7	1.3	470	5.25 ± 0.16	5.41
	After poling	10.4	0.92	56.7	1.1	439	5.46 ± 0.20	5.66
5%	Before poling	10.0	0.87	50.6	3.0	536	4.41 ± 0.15	4.56
	After poling	10.4	0.90	53.5	1.5	542	5.01 ± 0.18	5.19
18%	Before poling	**10.7**	**0.83**	**52.0**	**3.4**	**411**	**4.60 ± 0.14**	**4.74**
	After poling	**11.3**	**0.91**	**63.0**	**0.9**	**887**	**6.48 ± 0.16**	**6.64**
38%	Before poling	6.1	0.68	21.6	8.4	111	0.90 ± 0.20	1.10
	After poling	9.1	0.73	33.5	3.3	153	2.20 ± 0.21	2.41
50%	Before poling	1.7	0.57	12.5	19.2	127	0.12 ± 0.05	0.17
	After poling	9.1	0.71	31.8	8.0	333	2.04 ± 0.19	2.23

The NPs were precipitated out by the high speed centrifuge at a speed of 20 000 rpm for 10 min. The low temperature was used to lower the diffusion rate of the solvents and to stabilize the interfaces. The bottom solution below the interfacial layer containing the NPs was transferred to a flask and refluxed at 90 °C for 60 min to crystallize the as-grown NPs. The hot solution was cooled down to room temperature at the speed of 1 °C per minute. The P(VDF-TrFE) NP concentration was 2 mg mL^{-1}, which corresponded to 4.2×10^{12} particles mL^{-1}. The dispersion of the as-grown NPs was stable and could remain transparent for several weeks.

P(VDF-TrFE) NPs Characterization: A Quanta 200 FEG Environmental Scanning Electron Microscope (ESEM) using a field-emission gun (FEG) electron source was used to observe the size of the P(VDF-TrFE) NPs. The films with P(VDF-TrFE) NPs were first covered with a thin layer of gold coated using a Cressington 108 Auto Sputter Coater before the SEM measurement.

To characterize crystallinity of the P(VDF-TrFE) nanostructure, XRD measurements were performed with a Rigaku D/Max-B X-ray diffractometer with Bragg-Brentano parafocusing geometry, a diffracted beam monochromator, and a conventional copper target x-ray tube set to 40KV and 30 mA. The wavelength of the X-ray was 1.544 Å (Cu Kα,). To prepare the samples for XRD measurement, both as-grown P(VDF-TrFE) NPs and refluxed P(VDF-TrFE) NPs were spin coated on bare Si substrates layer by layer.

The topography of P(VDF-TrFE) NPs on an organic active layer surface was characterized by atomic force microscopy (AFM) (Multi-mode Nanoscope IIIA, Veeco Metrology Inc.) in the tapping mode using the tips with a force constant at 0.5–9.5 N m^{-1} (Nanosensors). The sample was prepared with spun NPs on top of a dry active layer at a speed of 2500 rpm for 60 s.

Ferroelectric Organic Photovoltaic (FE-OPV) Device Fabrication and Characterization: ITO substrates were treated by ultraviolent-ozone for 10 min. Poly(3,4-ethylenedioxythiophene)–polystyrenesulfonic acid (PEDOT:PSS, Baytron-P 4083) was then spun onto ITO substrates at a speed of 3000 rpm and heated at 130 °C for 30 min. PCDTBT:PC$_{70}$BM (1:4 w/w) was dissolved in an *o*-dichlorobenzene (DCB):chlorobenzene (CB) (3:1 V/V) mixed solution at a concentration of 4 mg mL^{-1} and stirred for 15 h at 40 °C. Then the mixed solution was spun on ITO/PEDOT:PSS substrates at a speed of 2400 rpm for 14 s, resulting in a thickness of about 80 nm. Then the P(VDF-TrFE) NPs were spun on top of dried PCDTBT:PC$_{70}$BM film under different spin rates for 60 s. The device was finished with thermal evaporate 100 nm aluminum (Al). The controlled device was evaporated with 20 nm Ca and 100 nm Al. The FE-OPV device was poled under negative bias under 120 °C for 10 s. All devices were measured under simulated AM 1.5G irradiation (100 mW cm^{-2}) with a xenon-lamp-based solar simulator and the Newport incident photon to charge carrier efficiency (IPCE).

[1] L. Dou, J. You, J. Yang, C. C. Chen, Y. He, S. Murase, T. Moriarty, K. Emery, G. Li, Y. Yang, *Nat. Photonics* **2012**, *6*, 180.
[2] X. Li, W. C. H. Choy, L. Huo, F. Xie, W. E. I. Sha, B. Ding, X. Guo, Y. Li, J. Hou, J. You, *Adv. Mater.* **2012**, *24*, 3046.
[3] C. E. Small, S. Chen, J. Subbiah, C. M. Amb, S. W. Tsang, T. H. Lai, J. R. Reynolds, F. So, *Nat. Photonics* **2011**, *6*, 115.
[4] Y. Sun, J. H. Seo, C. J. Takacs, J. Seifter, A. J. Heeger, *Adv. Mater.* **2011**, *23*, 1679.
[5] J. Huang, Z. Xu, Y. Yang, *Adv. Funct. Mater.* **2007**, *17*, 1966.
[6] Z. He, C. Zhong, X. Huang, W. Y. Wong, H. Wu, L. Chen, S. Su, Y. Cao, *Adv. Mater.* **2011**, *23*, 4636.
[7] Y. Zhou, C. Fuentes-Hernandez, J. Shim, J. Meyer, A. J. Giordano, H. Li, P. Winget, T. Papadopoulos, H. Cheun, J. Kim, *Science* **2012**, *336*, 327.
[8] M. O. Reese, M. S. White, G. Rumbles, D. S. Ginley, S. E. Shaheen, *Appl. Phys. Lett.* **2008**, *92*, 053307.
[9] Y. Yuan, T. J. Reece, P. Sharma, S. Poddar, S. Ducharme, A. Gruverman, Y. Yang, J. Huang, *Nat. Mater.* **2011**, *10*. 296.
[10] Y. Yuan, P. Sharma, Z. Xiao, S. Poddar, A. Gruverman, S. Ducharme, J. Huang, *Energy Environ. Sci.* **2012**, *5*, 8558.
[11] B. Yang, Y. Yuan, P. Sharma, S. Poddar, R. Korlacki, S. Ducharme, A. Gruverman, R. Saraf, J. Huang, *Adv. Mater.* **2012**, *24*, 1455.
[12] Y. Liang, Y. Wu, D. Feng, S. T. Tsai, H. J. Son, G. Li, L. Yu, *J. Am. Chem. Soc.* **2008**, *131*, 56.

ADVANCED
ENERGY
MATERIALS

www.advenergymat.de

Materials Views
www.MaterialsViews.com

COMMUNICATION

[13] W. Chen, T. Xu, F. He, W. Wang, C. Wang, J. W. Strzalka, Y. Liu, J. Wen, D. Miller, J. Chen, *Nano Lett.* **2011**, *11*, 3707.

[14] S. H. Park, A. Roy, S. Beaupré, S. Cho, N. Coates, J. S. Moon, D. Moses, M. Leclerc, K. Lee, A. J. Heeger, *Nat. Photonics* **2009**, *3*, 297.

[15] J. H. Seo, A. Gutacker, Y. Sun, H. Wu, F. Huang, Y. Cao, U. Scherf, A. Heeger, G. C. Bazan, *J. Am. Chem. Soc.* **2011**, *133*, 8416.

[16] D. H. Wang, J. S. Moon, J. Seifter, J. Jo, J. H. Park, O. Park, A. J. Heeger, *Nano Lett.* **2011**, *21*, 3163.

[17] J. Guo, Y. Liang, J. Szarko, B. Lee, H. J. Son, B. S. Rolczynski, L. Yu, L. X. Chen, *J. Phys. Chem. B* **2010**, *114*, 742.

[18] P. Sharma, T. J. Reece, S. Ducharme, A. Gruverman, *Nano Lett.* **2011**, *11*, 1970.

[19] Z. Hu, M. Tian, B. Nysten, A. M. Jonas, *Nat. Mater.* **2008**, *8*, 62.

[20] E. Edqvist, E. Hedlund, *J. Micromech. Microeng.* **2009**, *19*, 115019.

[21] P. J. Cottinet, D. Guyomar, M. Lallart, B. Guiffard, L. Lebrun, *IEEE Trans. Ultrasonics* **2011**, *58*, 1842.

[22] S. W. Choi, J. R. Kim, Y. R. Ahn, S. M. Jo, E. J. Cairns, *Chem. Mater.* **2007**, *19*, 104.

[23] C. C. Hong, S. Y. Huang, J. Shieh, S. H. Chen, *Macromolecules* **2012**, *45*, 1580.

[24] J. L. Lutkenhaus, K. McEnnis, A. Serghei, T. P. Russell, *Macromolecules* **2010**, *43*, 3844.

[25] M. C. García-Gutiérrez, A. Linares, J. J. Herŕndez, D. R. Rueda, T. A. Ezquerra, P. Poza, R. J. Davies, *Nano Lett.* **2010**, *10*, 1472.

[26] A. Serghei, J. L. Lutkenhaus, D. F. Miranda, K. McEnnis, F. Kremer, T. P. Russell, *Small* **2010**, *6*, 1822.

[27] Y. Yang, K. Mielczarek, M. Aryal, A. Zakhidov, W. Hu, *ACS Nano* **2012**, *6*, 2877.

[28] Y. Sun, C. J. Takacs, S. R. Cowan, J. H. Seo, X. Gong, A. Roy, A. J. Heeger, *Adv. Mater.* **2011**, *23*. 1679.

[29] T. P. Silverstein, *J. Chem. Educ.* **1998**, *75*, 116.

[30] K. Koga, N. Nakano, T. Hattori, H. Ohigashi, *J. Appl. Phys.* **1990**, *67*, 965.

[31] M. Bai, S. Ducharme, *Appl. Phys. Lett.* **2004**, *85*, 3528.

[32] S. Guo, X. Sun, S. Wang, S. Xu, X. Z. Zhao, H. L. W. Chan, *Mater. Chem. Phys.* **2005**, *91*, 348.

[33] J. Kim, Ph.D. Thesis, University of Nebraska-Lincoln, **2008**.

[34] P. A. C. Quist, T. J. Savenije, J. M. Schins, J. E. Kroeze, P. A. Rijkers, L. D. A. Siebbeles, *Phys. Rev. B* **2007**, *75*, 195317.

[35] C. H. Peters, I. Sachs-Quintana, J. P. Kastrop, S. Beaupré, M. Leclerc, M. D. McGehee, *Adv. Energy Mater.* **2011**, *1*, 491.